

Collective oscillations of a Fermi gas in the unitarity limit: Temperature effects and the role of pair correlations

S. Riedl,^{1,2} E. R. Sánchez Guajardo,¹ C. Kohstall,¹ A. Altmeyer,^{1,2} M. J. Wright,¹ J. Hecker Denschlag,¹ R. Grimm,^{1,2} G. M. Bruun,^{3,4} and H. Smith⁴

¹*Institut für Experimentalphysik und Zentrum für Quantenphysik, Universität Innsbruck, 6020 Innsbruck, Austria*

²*Institut für Quantenoptik und Quanteninformation, Österreichische Akademie der Wissenschaften, 6020 Innsbruck, Austria*

³*Dipartimento di Fisica, Università di Trento and CNR-INFM BEC Center, I-38050 Povo, Trento, Italy*

⁴*Niels Bohr Institute, University of Copenhagen, DK-2100 Copenhagen Ø, Denmark*

(Received 10 September 2008; published 5 November 2008)

We present detailed measurements of the frequency and damping of three different collective modes in an ultracold trapped Fermi gas of ${}^6\text{Li}$ atoms with resonantly tuned interactions. The measurements are carried out over a wide range of temperatures. We focus on the unitarity limit, where the scattering length is much greater than all other relevant length scales. The results are compared to theoretical calculations that take into account Pauli blocking and pair correlations in the normal state above the critical temperature for superfluidity. We show that these two effects nearly compensate each other and the behavior of the gas is close to that of a classical gas.

DOI: 10.1103/PhysRevA.78.053609

PACS number(s): 03.75.Ss, 67.10.Db, 34.50.Cx

I. INTRODUCTION

The study of collective oscillations in quantum liquids and gases has yielded a wealth of insights into the properties of strongly correlated systems. An early example concerning strongly correlated fermions is the observed transition from ordinary first sound to zero sound in the normal state of liquid ${}^3\text{He}$ as the temperature is lowered [1]. In this paper, we explore related phenomena in an ultracold quantum gas of fermions in the unitarity limit [2] by measuring three different collective modes under similar conditions. The frequency and damping of the modes exhibit the characteristic transition from hydrodynamic behavior at low temperature to collisionless behavior at higher temperature. The experimental observations are compared to theoretical model calculations that apply to the normal state of the gas above the critical temperature T_c for superfluidity. In the unitarity limit, the strongly correlated normal state between T_c and the Fermi temperature T_F is arguably not as well understood as the $T=0$ superfluid phase [3]. It is shown that the combined effects of temperature and pair correlations account for most of the observed features in this interesting temperature regime.

Our measurements of the collective modes are carried out for an elongated trap geometry, which has previously been shown to be well suited for studying the dynamical behavior of a strongly interacting Fermi gas [4–10]. We focus on two collective excitations of a cylindrically symmetric cigar-shaped cloud, namely, the radial compression mode and the radial quadrupole mode. In addition we study the scissors mode under conditions where the cloud exhibits pronounced ellipticity in the plane perpendicular to the direction of the cigar-shaped cloud. In all three modes, the cloud oscillates mainly in the plane normal to the direction of the cigar-shaped cloud. For a sketch of the modes, see Fig. 1.

Previous experiments on collective modes in a strongly interacting Fermi gas studied the effect of the interaction strength in the zero-temperature limit. [4–6,8,9]. Systematic

investigations were performed studying the radial compression mode [4,5,8] and the radial quadrupole mode [9]. Measurements on the compression mode served as a sensitive probe for the equation of state of the gas in the zero temperature limit throughout the crossover regime from the BCS regime to a Bose-Einstein condensate (BEC). In contrast to the compression mode, the frequency of the radial quadrupole mode allows one to test the hydrodynamic behavior without being influenced by the equation of state. This made it possible to investigate the transition from hydrodynamic to collisionless behavior with decreasing coupling strength of the atom pairs on the BCS side of the crossover.

While the hydrodynamic behavior in the zero-temperature limit is now well understood as a result of superfluidity, an understanding of the effects of temperature on the collective modes has remained a challenge. Only few experiments have so far addressed this problem [5,7,8,10]. Previously, the tem-

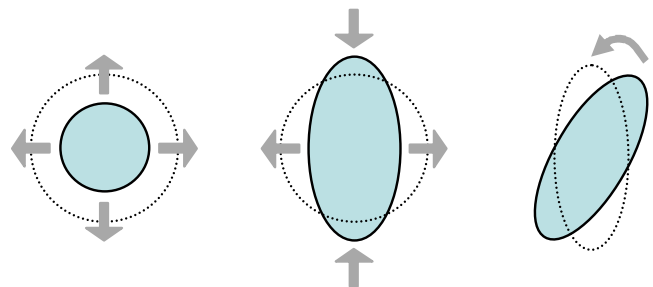


FIG. 1. (Color online) Sketch of the three collective modes investigated in this work: the compression mode, the quadrupole mode, and the scissors mode (from left to right). The oscillations take place in the plane of tight confinement, perpendicular to the direction of the elongated, cigar-shaped cloud. While the compression mode represents an oscillation of the overall cloud volume, the other two modes involve only surface deformations. Excitation of the quadrupole mode leads to an oscillating elliptic shape. The scissors mode appears as an angular oscillation of an elliptic cloud about a principal axis of an elliptic trap.

TABLE I. Trap parameters for the different modes.

	Compression	Quadrupole	Scissors
$\omega_x/2\pi$ (Hz)	1100	1800	1600
$\omega_y/2\pi$ (Hz)	1100	1800	700
$\omega_z/2\pi$ (Hz)	26	32	30
T_F (μ K)	1.8	2.7	1.9
V_0/k (μ K)	19	50	40

perature dependence of the radial compression mode [7] and the scissors mode was studied [10]. Our present experiments aim at addressing the open questions raised by the different results obtained in these experiments: The frequency and damping of the radial compression mode were studied as function of the temperature in experiments performed by Kinast *et al.* [7]. There the mode frequency appeared to stay close to the hydrodynamic value even for temperatures exceeding the Fermi temperature. This surprising finding stands in contrast to scissors mode measurements, performed later by Wright *et al.* [10], which clearly showed a transition to collisionless behavior in the same temperature range. Furthermore the data of [7] on the damping of the compression mode did not show a maximum as was seen in [10] for the scissors mode measurement. These apparent discrepancies are a particular motivation for our present study of different collective modes under similar experimental conditions.

II. EXPERIMENTAL PROCEDURE

The apparatus and the basic preparation methods for experiments with a strongly interacting Fermi gas of ${}^6\text{Li}$ atoms have been described in our previous work [11,12]. As a starting point, we produce a molecular BEC of ${}^6\text{Li}_2$. By changing the external magnetic field, we can control the interparticle interactions in the vicinity of a Feshbach resonance, which is centered at 834 G [13]. The measurements of the collective modes are performed at the center of the Feshbach resonance, where the interactions are unitarity limited.

The atoms are confined in an elongated, nearly harmonic trapping potential, where the trap frequencies ω_x and ω_y in the transverse direction are much larger than the axial trap frequency ω_z . The confinement in the transverse direction is created by an optical dipole trap using a focused 1030 nm laser beam with a waist of 47 μm . Note that the Gaussian shape of the laser beam leads to significant anharmonicities in the trapping potential. The potential in the axial direction consists of a combination of optical and magnetic confinement; the magnetic confinement is dominant under the conditions of the present experiments. The trap parameters, given in Table I, represent a compromise between trap stability and anharmonic effects [14]. The Fermi temperature is given by $T_F = E_F/k$, where the Fermi energy $E_F = \hbar(3N\omega_x\omega_y\omega_z)^{1/3} = \hbar^2 k_F^2/2m$, k_F is the Fermi wave number, and k is the Boltzmann constant. The parameter V_0 is the trap depth, and N is the total number of atoms, given by $N=6 \times 10^5$. The interactions are characterized by the dimensionless parameter $1/k_F a$, where a is the s -wave scattering length.

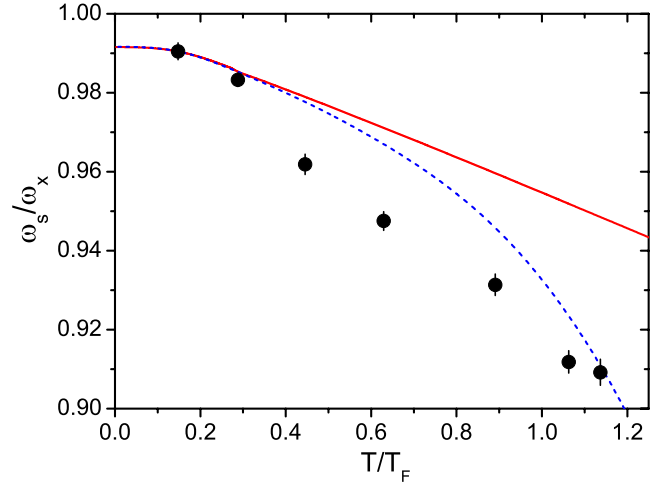


FIG. 2. (Color online) Sloshing mode frequency ω_s normalized by the trap frequency ω_x as a function of temperature. The measured frequency shows a decrease with increasing temperature (dots), which is due to the increase in the size of the cloud. The lines show the expected frequency from a first-order anharmonic correction; see Appendix B. To determine the cloud size for different temperatures we assume a harmonic potential (solid line) and a Gaussian potential (dashed line), respectively [15].

To control the aspect ratio ω_x/ω_y , we use rapid spatial modulation of the trapping beam by two acousto-optical deflectors, resulting in the creation of time-averaged trapping potentials [9]. This, on one hand, allows us to compensate for residual ellipticity of the trapping potential on the percent level and thus to realize a cylindrical symmetric trap ($\omega_x = \omega_y$). On the other hand, it allows for the excitation of surface modes by deliberate introduction of elliptic trapping potentials ($\omega_x \neq \omega_y$). The procedures used to excite the modes are outlined in Appendix A. To change the temperature we apply a controlled heating scheme via sudden compression of the gas as described in [10]. Detection of the cloud is done by absorption imaging which displays the shape of the cloud in the x - y plane after expansion. For each mode under investigation we determine the frequency and damping following the procedures of our previous work [8–10]; see also Appendix A.

Because of the Gaussian shape of the trapping potential, corrections are needed for a precise comparison of the experimental observation to the idealized case of perfect harmonic trapping. Especially for higher temperatures, when the size of the cloud is larger, anharmonic corrections become important. This is demonstrated by measurements of the transverse sloshing mode frequency ω_s (Fig. 2), which clearly show a substantial decrease with increasing temperature. To reduce the anharmonic effects on the frequencies of the collective modes under investigation, we normalize the compression and quadrupole collective mode frequencies to the sloshing mode frequency in the transverse direction. This normalization reduces the anharmonic effects to a large extent since the decrease of the sloshing mode frequency with increasing cloud size is of the same order as the corresponding decrease of the frequency of the transverse modes [16]. To normalize the scissors mode frequency, we take the geo-

metric average of the two different sloshing mode frequencies in the transverse direction.

For each of the trap parameters of the different modes we determine the sloshing mode frequency as a function of the temperature. As an example, we show ω_s for the trap parameters used for the compression mode measurement; see Fig. 2. We compare ω_s/ω_x (dots) to a theoretical model which allows us to calculate the sloshing frequency as a function of the cloud size; see Appendix B. Assuming a harmonic potential to derive the mean squared size $\langle x^2 \rangle$ [15] underestimates the anharmonic effects (solid line), in particular for higher temperatures. Taking into account a Gaussian potential to determine $\langle x^2 \rangle$ (dashed line) gives results that agree much better with the measured sloshing frequency.

Since the purpose of this paper is a comparative study of different collective modes and not the precision measurement of a single mode as in previous work [8], we follow a faster yet simpler procedure to normalize the frequencies. We measure the sloshing mode frequency only at particular temperatures of interest. From these points we determine the temperature dependence of the sloshing frequency by interpolation. Even though the normalization takes into account the temperature dependence of the anharmonicity, it does not reduce effects due to drifts in the power of the trapping beam. We believe this to be the main source for the scatter of the data in Fig. 4.

To determine the temperature of the gas, we first adiabatically change the magnetic field to 1132 G [17], where $1/k_F a \approx -1$, to reduce the effect of interactions on the density distribution [18]. Under this condition, for $T > 0.2T_F$, the interaction effect on the density distribution is sufficiently weak to treat the gas as a noninteracting one to determine the temperature from time-of-flight images. We fit the density distribution after 2 ms release from the trap to a finite-temperature Thomas-Fermi profile. The temperature measured at 1132 G is converted to the temperature in the unitarity regime under the assumption that the conversion takes place isentropically, following the approach of Ref. [19]. Statistical uncertainties for the temperature stay well below $0.05T_F$.

III. THEORY

We shall compare our experimental findings to the results of model calculations that apply to the normal state of the gas, i.e., at temperatures above T_c . In this section, we outline our theoretical approach to the calculation of mode frequencies for $T > T_c$. A more detailed description can be found in Refs. [20,21]. We assume that single-particle excitations are reasonably well defined in the sense that most of the spectral weight of the single-particle spectral function is located at a peak corresponding to that of noninteracting particles. The low-energy dynamics of the gas can then be described by a semiclassical distribution function $f(\mathbf{r}, \mathbf{p}, t)$ which satisfies the Boltzmann equation. A collective mode corresponds to a deviation $\delta f = f - f^0$ away from the equilibrium distribution $f^0(\mathbf{r}, \mathbf{p})$. Writing $\delta f(\mathbf{r}, \mathbf{p}, t) = f^0(\mathbf{r}, \mathbf{p})[1 - f^0(\mathbf{r}, \mathbf{p})]\Phi(\mathbf{r}, \mathbf{p}, t)$ and linearizing the Boltzmann equation in $\delta f(\mathbf{r}, \mathbf{p}, t)$ yields

$$f^0(1 - f^0) \left(\frac{\partial \Phi}{\partial t} + \dot{\mathbf{r}} \cdot \frac{\partial \Phi}{\partial \mathbf{r}} + \dot{\mathbf{p}} \cdot \frac{\partial \Phi}{\partial \mathbf{p}} \right) = -I[\Phi], \quad (1)$$

where $\dot{\mathbf{r}} = \mathbf{v} = \mathbf{p}/m$, $\dot{\mathbf{p}} = -\partial V/\partial \mathbf{r}$, and I is the collision integral. We take the potential $V(\mathbf{r})$ to be harmonic and given by $V(\mathbf{r}) = m(\omega_x^2 x^2 + \omega_y^2 y^2 + \omega_z^2 z^2)/2$.

To describe the collective modes we expand the deviation function in a set of basis functions ϕ_i according to

$$\Phi(\mathbf{r}, \mathbf{p}, t) = e^{-i\omega t} \sum_i c_i \phi_i(\mathbf{r}, \mathbf{p}), \quad (2)$$

where ω is the mode frequency. For the compression mode with a velocity field $\mathbf{v} \propto (x, y, cz)$, with c a constant, we use the functions

$$\phi_1 = x^2 + y^2, \quad \phi_2 = xp_x + yp_y, \quad \phi_3 = p_x^2 + p_y^2, \quad \phi_4 = p_z^2. \quad (3)$$

For the quadrupole mode with a velocity field $\mathbf{v} \propto (x, -y, 0)$ (ignoring the small velocity along the axial direction), we use

$$\phi_1 = x^2 - y^2, \quad \phi_2 = xp_x - yp_y, \quad \phi_3 = p_x^2 - p_y^2, \quad (4)$$

whereas the basis functions for the scissors mode are given in Ref. [22]. Our choice of basis functions is physically motivated by the characteristic features of the three different modes illustrated in Fig. 1. Since we limit ourselves to a few simple functions, the basis sets are not complete, but we do not expect qualitative changes to occur as a result of including more basis functions in our calculation.

We now insert the expansion (2) into (1) and take moments by multiplying with the functions ϕ_i and integrating over both \mathbf{r} and \mathbf{p} . This yields a set of linear equations for the coefficients c_i for each of the collective modes. The corresponding determinants give the mode frequencies. For the compression mode, we obtain

$$i\omega(\omega^2 - 4\omega_\perp^2) + \frac{1}{\tau} \left(\frac{10}{3} \omega_\perp^2 - \omega^2 \right) = 0, \quad (5)$$

and for the quadrupole mode, we get

$$i\omega(\omega^2 - 4\omega_\perp^2) + \frac{1}{\tau} (2\omega_\perp^2 - \omega^2) = 0. \quad (6)$$

The equation for the scissors mode is given in Ref. [22].

The effective collision rate $1/\tau$ in (5) and (6) is given by

$$\frac{1}{\tau} = \frac{\int d^3r d^3p p_x p_y I[p_x p_y]}{\int d^3r d^3p p_x^2 p_y^2 f^0(1 - f^0)}. \quad (7)$$

Note that this expression for $1/\tau$ involves a spatial average over the cloud. In the collisionless limit, $\omega\tau \gg 1$, the two equations (5) and (6) both yield $\omega = 2\omega_\perp$, where $\omega_\perp = \omega_x = \omega_y$, while in the hydrodynamic limit, $\omega\tau \ll 1$, they result in $\omega = \sqrt{10/3}\omega_\perp$ for the compression mode and $\omega = \sqrt{2}\omega_\perp$ for the quadrupole mode.

The dependence on temperature T and scattering length a enters through τ . In particular, Pauli blocking and pair cor-

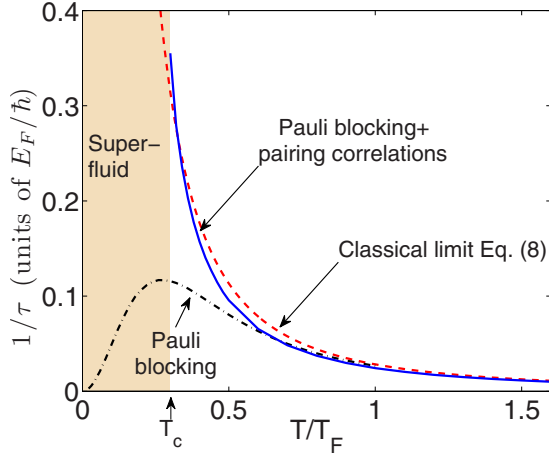


FIG. 3. (Color online) Effective collision rate for a gas in the unitarity limit. The dashed curve is the classical result, the dashed-dotted includes Pauli blocking, and the solid line includes pairing correlations in the scattering matrix. The superfluid region for $T < T_c$ is indicated.

relations strongly depend on T and a , and we now examine their role on the effective collision rate. In Fig. 3, we plot $1/\tau$ as a function of temperature for a gas in the unitarity limit $|a| \rightarrow \infty$ using three different approximations for the collision integral. First, the dashed curve gives the effective collision rate in the classical regime using the vacuum expression $\mathcal{T}_{\text{vac}} = \mathcal{T}_0 / (1 + iqa)$ for the scattering matrix with $\mathcal{T}_0 = 4\pi\hbar^2 a/m$. The s -wave differential cross section $d\sigma/d\Omega$ which enters in the collision integral I is related to the scattering T matrix by $d\sigma/d\Omega = m^2 |T|^2 / (4\pi\hbar^2)^2$. In the classical regime, we then get from (7)

$$\frac{1}{\tau_{\text{class}}} = \frac{4}{45\pi} \frac{kT_F T_F^2}{\hbar T^2} \quad (8)$$

for a gas in the unitarity limit [22]. The small prefactor $4/(45\pi) \approx 0.028$ in (8) implies that the effective collision rate is significantly smaller than what one would expect from simple estimates or dimensional analysis at unitarity. Second, the dashed-dotted curve gives the effective collision rate when Pauli blocking effects are included as in [20], while we still use the vacuum expression \mathcal{T}_{vac} for the scattering matrix. Pauli blocking effects reduce the available phase space for scattering, thereby reducing the scattering rate. For $T \ll T_F$ Pauli blocking in a normal Fermi system gives $1/\tau \propto T^2$. Finally, we plot as a solid curve in Fig. 3 the effective collision rate, taking into account both Pauli blocking and many-body effects for \mathcal{T} in the ladder approximation, which includes the Cooper (pairing) instability. This gives $\mathcal{T} = \mathcal{T}_0 / (1 - \mathcal{T}_0 \Pi)$ where Π is the pair propagator. Since our treatment of the pair correlations applies only to the normal state of the gas, we plot this curve for temperatures greater than the critical temperature T_c , which within the ladder approximation used here is given by $T_c \approx 0.3T_F$ for a trap [21].

We see that $1/\tau$ is increased by the pairing correlations for the \mathcal{T} matrix. The pairing correlations significantly increase the effective collision rate for temperatures $(T - T_c)/T_c \lesssim 1$ [21]. One often refers to this temperature range

as the pseudogap regime. In fact, pairing correlations almost cancel the Pauli blocking effect in the collision integral above T_c , and $1/\tau$ is fairly accurately given by the classical value as can be seen from Fig. 3. At high temperatures, this cancellation can be demonstrated analytically by carrying out a high-temperature expansion of (7). We obtain after some algebra the simple expression

$$\frac{1}{\tau} = \frac{1}{\tau_{\text{class}}} \left[1 + \frac{1}{32} \left(\frac{T_F}{T} \right)^3 \right]. \quad (9)$$

The presence of the small prefactor $1/32$ in (9) shows that the leading correction to the classical limit is less than 3% at temperatures above the Fermi temperature T_F .

IV. RESULTS AND DISCUSSION

The theoretical results of the previous section were all obtained for a purely harmonic potential. Since anharmonicity plays an important role in our experiments, as discussed in Sec. II, we normalize the measured frequencies and damping rates for the collective modes to the measured temperature-dependent sloshing frequencies, for which an example is shown in Fig. 2. In the following we compare our observations to the theoretical results. It should be emphasized that the theoretical expressions for the frequency and damping contain no free parameters to fit theory and experiment.

First we discuss the frequency for the three modes under investigation as a function of the temperature, as plotted in Fig. 4. In all three cases the theoretical expression for the frequency (the full lines in Fig. 4) smoothly changes from the hydrodynamic value at the lowest temperature considered to the collisionless value at high temperatures. The normalized frequencies in the hydrodynamic limit for the quadrupole mode and compression mode are $\sqrt{2} \approx 1.41$ and $\sqrt{10/3} \approx 1.83$, respectively. The normalized frequency in the collisionless limit for both these modes is 2. Using the geometric average of the trap frequencies to normalize the scissors mode frequency, one gets, using the ratio $\omega_x/\omega_y = 16/7$ from Table I, that $\sqrt{(\omega_x^2 + \omega_y^2)/(\omega_x \omega_y)} \approx 1.65$ in the hydrodynamic limit and $(\omega_x + \omega_y)/\sqrt{\omega_x \omega_y} \approx 2.17$ in the collisionless limit. Note that the scissors mode consists of a two-frequency oscillation in the collisionless limit. Here we consider only the larger-frequency component. The lower-frequency component exhibits increasing damping toward lower temperatures and disappears in the hydrodynamic limit [23].

Figure 4 illustrates that there is a reasonable overall agreement between experiment and theory, although some differences exist. The agreement is best for the scissors mode, while for the quadrupole mode the changeover from hydrodynamic to collisionless behavior happens at a lower temperature than the one found theoretically. The measured compression mode frequency, which shows considerable scatter, increases with increasing temperature and is close to the collisionless value at the highest temperature measured.

The observed change from the hydrodynamic to the collisionless frequency for the compression mode is in contrast

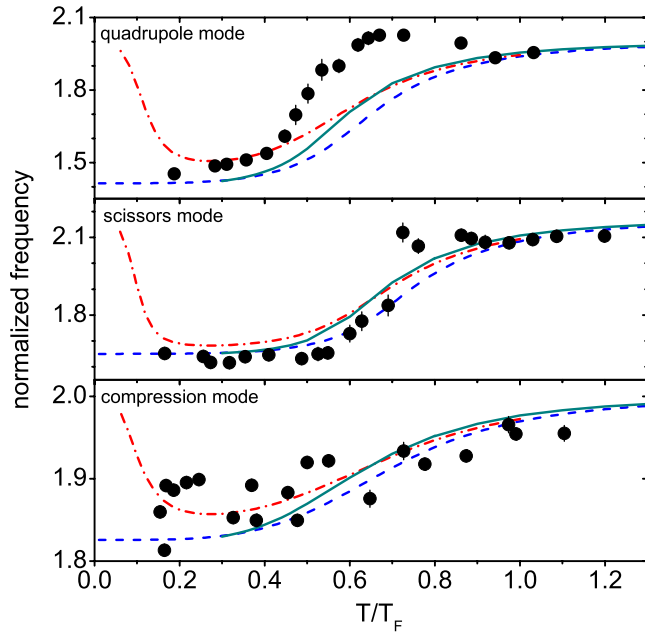


FIG. 4. (Color online) Observed normalized mode frequencies versus temperature for the quadrupole mode, the scissors mode, and the compression mode. The error bars indicate the statistical error of a single frequency measurement. The full lines are the result of the theory for the normal state described in Sec. III, which includes the combined effects of Pauli blocking and pair correlations; note that these curves start at $T=0.3T_F$, which in the ladder approximation used here is the transition temperature to the superfluid state. For illustrative purposes we also show the theoretical results when only Pauli blocking is taken into account (dashed-dotted lines) and those for a classical gas (dashed lines).

to Ref. [7], where the frequency remains close to the hydrodynamic value for the same temperature range. We attribute this discrepancy to different treatments of anharmonic effects, which are particularly important for this mode since the difference between the hydrodynamic and collisionless frequency is of the same order as the frequency shift due to anharmonic effects. In Ref. [7] the data are corrected by including anharmonic effects to first order, while we adopt the point of view that the main anharmonic effects can be taken into account by normalizing the measured oscillation frequencies to the measured temperature-dependent sloshing frequencies. Figure 2 illustrates that a simple first-order treatment of anharmonic effects on the sloshing frequency does not account quantitatively for the observed variation with temperature.

At very low temperatures the measured frequencies are close to the hydrodynamic values because the gas is in the superfluid phase [8,9]. Without pair correlations, but with Pauli blocking, at these low temperatures the frequencies would assume their collisionless values as illustrated by the dash-dotted lines in Fig. 4.

We now proceed to consider the damping of the oscillations. The experimental values for the normalized damping rate are shown in Fig. 5. Theoretically, one expects the damping to vanish in the hydrodynamic and collisionless

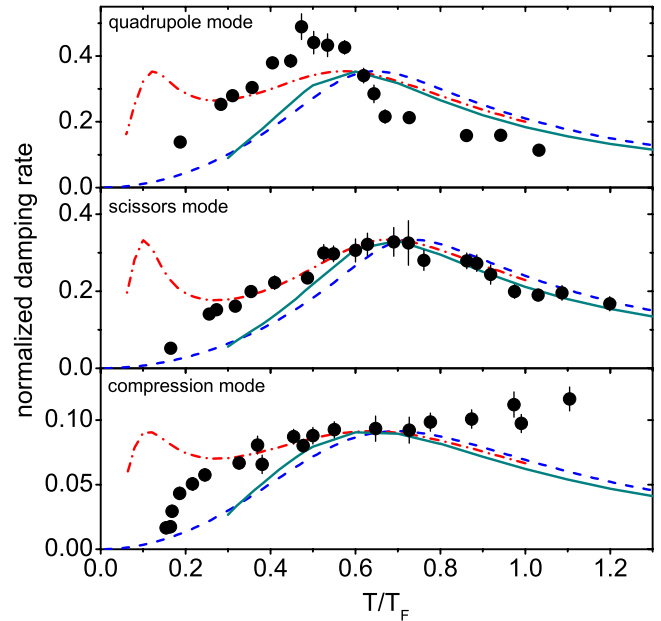


FIG. 5. (Color online) Normalized mode damping versus temperature for the quadrupole mode, the scissors mode, and the compression mode. The points are experimental values, while the full lines represent our calculated values, taking into account both Pauli blocking and pairing effects. The dashed-dotted line takes only Pauli blocking into account, while the dashed line is the classical (high-temperature) result.

limits and exhibit a maximum in between, as brought out by the calculations in Sec. III. Experimentally, both the quadrupole and the scissors mode exhibit the expected maximum in damping in the transition region. For the compression mode, however, the damping does not decrease at higher temperatures. This surprising behavior for the compression mode has already been found in [7]. A possible reason for the increasing damping is dephasing-induced damping due to anharmonicity. Anharmonic effects are more important for the compression mode as the intrinsic damping is relatively small due to the small difference between the frequencies in the collisionless and hydrodynamic limits [24]. In contrast to the case of frequency discussed above, we cannot expect to take into account the main effects of anharmonicity by normalizing the measured damping rate to the temperature-dependent sloshing mode frequencies. This makes it delicate to compare our experimental results to those of a theory based on a purely harmonic potential. The damping of the quadrupole mode shows the expected qualitative behavior, although the maximum in damping happens at a lower temperature compared to theory. This is consistent with the frequency data for this mode, since the transition there also happens at lower temperature. For the scissors mode the experimental data agree fairly well with theory, although some discrepancy exists at the lowest temperatures.

We can relate the frequency and damping of the quadrupole mode directly to each other by eliminating the collision rate $1/\tau$ in (6). Writing $\omega = \omega_Q - i\Gamma_Q$ for the solution of (6) with ω_Q and Γ_Q being the quadrupole frequency and damping, we obtain

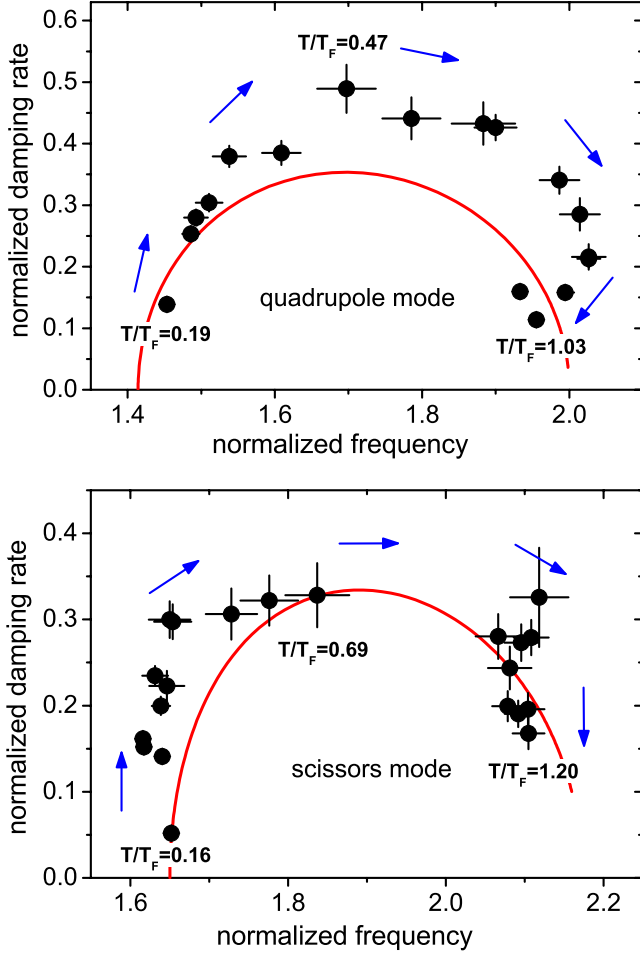


FIG. 6. (Color online) Normalized mode damping versus normalized frequency for the quadrupole and scissors modes. The solid line shows the expected behavior for a harmonic trap. The arrows point toward the direction of increasing temperature.

$$\Gamma_Q = \sqrt{-\omega_{\perp}^2 - \omega_Q^2 + \sqrt{8\omega_Q^2 - 7\omega_{\perp}^2}}. \quad (10)$$

A similar relation holds for the two other modes. This allows us to compare theory and experiment independently of any approximations involved in the evaluation of $1/\tau$. Figure 6 shows the normalized damping rate versus the normalized frequency of the quadrupole and the scissors mode; we do not show the data for the compression mode because of the apparent problems discussed before. We find that the maximum damping of the quadrupole mode is larger than expected. For the scissors mode the damping is larger only at low frequencies. This suggests that the difference between theory and experiment is not a consequence of the approximations entering the calculation of the relaxation rate but could be due to anharmonic effects or the need for larger basis sets to describe the modes [see (3) and (4)].

V. CONCLUSION

In this work we have presented measurements of the frequency and damping of three different collective modes under similar conditions for an ultracold Fermi gas of ${}^6\text{Li}$ at-

oms in the unitarity limit. The experimental results obtained in the normal state of the gas are in reasonable agreement with our theoretical calculations, which take into account Pauli blocking and pair correlations. The remaining discrepancies may originate in a variety of sources such as our treatment of anharmonic effects, the temperature calibration, and the use of a restricted basis for solving the Boltzmann equation. Also they may reflect the need to incorporate further interaction effects in the kinetic equation, which forms the starting point for the theoretical calculations. For instance, there are self-energy shifts on the left-hand side of the kinetic equation which could be important. The study of collective modes is a sensitive probe of the properties of strongly interacting particles such as the gas of ${}^6\text{Li}$ atoms under investigation, and further work on temperature-dependent phenomena will undoubtedly shed more light on these interesting many-body systems.

ACKNOWLEDGMENTS

We acknowledge support by the Austrian Science Fund (FWF) within SFB 15 (Project Part 21). M.J.W. was supported by a Marie Curie Action within the Sixth European Community Framework Program. Fruitful discussions with S. Stringari are appreciated. We thank Q. Chen and K. Levin for providing us with density profiles and temperature calibration curves.

APPENDIX A

Here we present more details of the experimental procedures used to excite the three collective modes. To excite the radial quadrupole mode we adiabatically deform the radially symmetric trap to an elliptic shape while keeping the average trap frequency constant before turning off the deformation suddenly [9]. The deformation is chosen such that the amplitude of the mode oscillation relative to the cloud size is below 10%. A two-dimensional Thomas-Fermi profile is fitted to the images, taken after a short expansion time of 0.5 ms. The difference in the width of the main axes is determined for different hold times and fitted to a damped sine function, from which we determine the frequency and damping of the mode.

The excitation of the radial compression mode is done by a sudden compression of the cloud. To determine the frequency and damping of the compression mode we follow the same procedure as for the quadrupole mode but fitting to the sum of the widths. Here we use an expansion time of 2 ms before taking the image.

The scissors mode appears as an angular oscillation of an elliptic cloud about a principal axis of an elliptic trap. To excite this oscillation we create an elliptic trap in the x - y plane and suddenly rotate the angle of the principal axes by 5° [10]. The tilt of the principal axes of the cloud is determined 0.8 ms after releasing the cloud from the trap for different hold times. If the gas is hydrodynamic, we fit a single damped sine function to the oscillation of the angle. However, for a collisionless gas, the oscillation exhibits two frequencies. Thus we fit a sum of two damped sine functions

each with their own free parameters. When the behavior changes from hydrodynamic to collisionless the single damped sine function fits the data reasonably well, as discussed in [10]. Since the larger of the two frequencies in the collisionless regime smoothly connects to the hydrodynamic frequency at low temperatures we only consider this frequency in the paper.

APPENDIX B

Here we briefly discuss the calculation of the transverse sloshing modes including anharmonic corrections to lowest order. The transverse trapping potential is

$$V(x,y) = V_0(1 - e^{-x^2/a^2 - y^2/b^2}) \\ \approx V_0 \left(\frac{x^2}{a^2} + \frac{y^2}{b^2} - \frac{x^4}{2a^4} - \frac{y^4}{2b^4} - \frac{x^2y^2}{a^2b^2} \right). \quad (\text{B1})$$

Concentrating without loss of generality on the sloshing mode in the x direction, we choose the function $\Phi = c_1x + c_2p_x$. Putting this into the linearized Boltzmann equation (1), eliminating c_2 , and taking the moment $\int dx dy n(x,y)$ with $n(x,y)$ the density (we ignore the axial direction), we obtain for the sloshing frequency

$$\omega_s^2 = \omega_x^2 \left(1 - \frac{m\omega_x^2 \langle x^2 \rangle + m\omega_y^2 \langle y^2 \rangle}{2V_0} \right). \quad (\text{B2})$$

Here $\langle x^2 \rangle = \int n(x,y)x^2 dx dy / \int n(x,y) dx dy$ and we have used $\omega_x^2 = 2V_0/ma^2$ together with $\omega_y^2 = 2V_0/b^2$.

-
- [1] W. R. Abel, A. C. Anderson, and J. C. Wheatley, *Phys. Rev. Lett.* **17**, 74 (1966).
- [2] *Ultracold Fermi Gases*, Proceedings of the International School of Physics “Enrico Fermi,” Course CLXIV, Varenna, 2006, edited by M. Inguscio, W. Ketterle, and C. Salomon (IOS Press, Amsterdam, 2008).
- [3] S. Giorgini, L. P. Pitaevskii, and S. Stringari, *Rev. Mod. Phys.* **80**, 1215 (2008).
- [4] M. Bartenstein, A. Altmeyer, S. Riedl, S. Jochim, C. Chin, J. Hecker Denschlag, and R. Grimm, *Phys. Rev. Lett.* **92**, 203201 (2004).
- [5] J. Kinast, S. L. Hemmer, M. E. Gehm, A. Turlapov, and J. E. Thomas, *Phys. Rev. Lett.* **92**, 150402 (2004).
- [6] J. Kinast, A. Turlapov, and J. E. Thomas, *Phys. Rev. A* **70**, 051401(R) (2004).
- [7] J. Kinast, A. Turlapov, and J. E. Thomas, *Phys. Rev. Lett.* **94**, 170404 (2005).
- [8] A. Altmeyer, S. Riedl, C. Kohstall, M. J. Wright, R. Geursen, M. Bartenstein, C. Chin, J. Hecker Denschlag, and R. Grimm, *Phys. Rev. Lett.* **98**, 040401 (2007).
- [9] A. Altmeyer, S. Riedl, M. J. Wright, C. Kohstall, J. Hecker Denschlag, and R. Grimm, *Phys. Rev. A* **76**, 033610 (2007).
- [10] M. J. Wright, S. Riedl, A. Altmeyer, C. Kohstall, E. R. Sánchez Guajardo, J. Hecker Denschlag, and R. Grimm, *Phys. Rev. Lett.* **99**, 150403 (2007).
- [11] S. Jochim, M. Bartenstein, A. Altmeyer, G. Hendl, S. Riedl, C. Chin, J. Hecker Denschlag, and R. Grimm, *Science* **302**, 2101 (2003).
- [12] M. Bartenstein, A. Altmeyer, S. Riedl, S. Jochim, C. Chin, J. Hecker Denschlag, and R. Grimm, *Phys. Rev. Lett.* **92**, 120401 (2004).
- [13] M. Bartenstein, A. Altmeyer, S. Riedl, R. Geursen, S. Jochim, C. Chin, J. Hecker Denschlag, R. Grimm, A. Simoni, E. Tiesinga, C. J. Williams, and P. S. Julienne, *Phys. Rev. Lett.* **94**, 103201 (2005).
- [14] Anharmonic effects depend on the ratio between the Fermi energy and trap depth E_F/V_0 [16]. Reducing this ratio decreases the anharmonic effects. This can be done by increasing the power of the trapping beam since E_F increases more slowly than V_0 . On the other hand technical reasons cause heating rates and larger drifts in the trap depth with increasing power.
- [15] Our calculation of $\langle x^2 \rangle$ is based on density profiles derived Ref. [19].
- [16] S. Stringari (private communication).
- [17] This is the largest magnetic field for which we can take absorption images in our present setup.
- [18] L. Luo, B. Clancy, J. Joseph, J. Kinast, and J. E. Thomas, *Phys. Rev. Lett.* **98**, 080402 (2007).
- [19] Q. Chen, J. Stajic, and K. Levin, *Phys. Rev. Lett.* **95**, 260405 (2005).
- [20] P. Massignan, G. M. Bruun, and H. Smith, *Phys. Rev. A* **71**, 033607 (2005).
- [21] G. M. Bruun and H. Smith, *Phys. Rev. A* **72**, 043605 (2005).
- [22] G. M. Bruun and H. Smith, *Phys. Rev. A* **76**, 045602 (2007).
- [23] D. Guéry-Odelin and S. Stringari, *Phys. Rev. Lett.* **83**, 4452 (1999).
- [24] D. Guéry-Odelin, F. Zambelli, J. Dalibard, and S. Stringari, *Phys. Rev. A* **60**, 4851 (1999).